INDONESIAN JOURNAL ON GEOSCIENCE
Geological Agency
Ministry of Energy and Mineral Resources

Journal homepage: http://ijog.geologi.esdm.go.id
ISSN 2355-9314, e-ISSN 2355-9306

Advanced Applications of Synthetic Aperture Radar (SAR) Remote Sensing for Detecting Pre- and Syn-eruption Signatures at Mount Sinabung, North Sumatra, Indonesia

Asep Saepuloh[1,2*], Prima Rizky Mirelva[1,3], and Ketut Wikantika[1,2]

[1]Centre for Remote Sensing, Bandung Institute of Technology (ITB)
Jln. Ganesha No. 10, Bandung, Indonesia. 40132
[2]Faculty of Earth Sciences and Technology, Bandung Institute of Technology (ITB)
Jln. Ganesha No. 10, Bandung, Indonesia. 40132
[3]Graduate School of Agriculture Sciences, Tottori University
4-101 Koyama Minami, Tottori, Japan. 680-8553

Corresponding author: saepuloh@gl.itb.ac.id
Manuscript received: November, 25, 2017; revised: December, 11, 2017;
approved: April, 12, 2019; available online: May, 22, 2019

Abstract - Mount Sinabung was re-activated at August 28th, 2010 after a long repose interval. The early stage of a phreatic eruption was then followed by magmatic eruptions at September 15th, 2013 for years until now. To understand the ground surface changes accompanying the eruption periods, comprehensive analyses of surface and subsurface data are necessary, especially the condition in pre- and syn-eruption periods. This study is raised to identify ground surface and topographical changes before, intra, and after the eruption periods by analyzing the temporal signature of surface roughness, moisture, and deformation derived from Synthetic Aperture Radar (SAR) data. The time series of SAR backscattering intensity were analyzed prior to and after the early eruption periods to know the lateral ground surface changes including estimated lava dome roughness and surface moisture. Meanwhile, the atmospherically corrected Differential Interferometric SAR (D-InSAR) method was also applied to know the vertical topographical changes prior to the eruptions. The atmospheric correction based on modified Referenced Linear Correlation (mRLC) was applied to each D-InSAR pair to exclude the atmospheric phase delay from the deformation signal. The changes of surface moistures on syn-eruptions were estimated by calculating dielectric constant from SAR polarimetric mode following Dubois model. Twenty-one Phased Array type L-band SAR (PALSAR) data on board Advanced Land Observing Satellite (ALOS) and nine Sentinel-1A SAR data were used in this study with the acquisition date between February 2006 and February 2017. For D-InSAR purposes, the ALOS PALSAR data were paired to generate twenty interferograms. Based on the D-InSAR deformation, three times inflation-deflation periods were observed prior to the early eruption at August 28th 2010. The first and second inflation-deflation periods at the end of 2008 and middle 2009 presented migration of magma batches and dike generations in the deep reservoir. The third inflation-deflation periods in the middle of 2010 served as a precursor signal presenting magma feeding to the shallow reservoir. The summit was inflated about 1.4 cm and followed by the eruptions. The deflation of about 2.3 cm indicated the release pressure and temperature in the shallow reservoir after the early eruption at August 28th, 2010. The last inflation-deflation period was also confirmed by the increase of the lava dome roughness size from 5,121 m^2 on July to 6,584 m^2 on August. The summit then inflated again about 1.1 cm after the first eruption and followed by unrest periods presented by lava dome growth and destruction at September 15th, 2013. The volcanic products including lava and pyroclastics strongly affected the moisture of surface layer. The volcanic products were observed to reduce the surface moisture within syn-eruption periods. The hot materials are presumed responsible for the evaporation of the surface moisture as well.

Keywords: ALOS PALSAR, Sentinel-1A, D-InSAR, surface moisture, Mount Sinabung

How to cite this article:
Saepuloh, A., Mirelva, P.R., and Wikantika, K., 2019. Advanced Applications of Synthetic Aperture Radar (SAR) Remote Sensing for Detecting Pre- and Syn-eruption Signatures at Mount Sinabung, North Sumatra, Indonesia. *Indonesian Journal on Geoscience*, 6 (2), p.123-140. DOI: 10.17014/ijog.6.2.123-140

Introduction

Indonesia is composed of 127 active volcanoes, and the 31 most active volcanoes are located on two of the most populated islands: Sumatra and Java. One of the active volcanoes in Sumatra is Mount Sinabung which re-activated in 2010 after a long dormancy. The latest magmatic eruption produced pyroclastic flow deposits indicated at 1,200 years B.P. by carbon dating (Sutawidjaja *et al*., 2013). The 2010 eruptions were followed by extensive damage on crop fields near the volcano, and almost twelve thousand people were evacuated to Kabanjahe Subregency(Nugroho, 2013). The early eruption was initiated by phreatic eruptions at August 28th, 2010 (Iguchi *et al*., 2012; Sutawidjaja *et al*., 2013). The eruption was then followed by magmatic eruptions in 2013 prolong activity to about seven year unrest (Gunawan *et al*., 2017; Nugraha *et al*., 2017). Thus, observing the first eruption phenomenon in the geological point of view and topographical change will be the key point to understand the cause and effect of the eruptions as well as for further purposes such as hazard and mitigation. The limited ground monitoring data prior to the 2010 eruption caused the eruption seem to be no precursory signal (Gunawan *et al*., 2017). Therefore, this paper demonstrated detection precursor signal to the eruption using satellite imageries.

Continuous observations were crucial to detect the precursors of an eruption such as geophysical and geochemical monitoring, encompassing seismic, ground deformation, gravity, magnetic, gas monitoring, as well as remote sensing (Martí and Ernst, 2005). The topographical change and ground deformation are the main precursory parameter in monitoring volcanic activities that remote sensing could be utilized. In this paper, the precursor signatures using Synthetic Aperture Radar (SAR) remote sensing techniques were extensively tried to recover including backscattering and phase data analyses related to changes of summit lava dome roughness and deformation signatures, respectively. Roughness of the ground surface is a physical parameter which is important for characterizing surface geology such as weathering and hydrothermal alteration degrees (Saepuloh *et al.*, 2015b).

The Differential Interferometric Synthetic Aperture Radar (D-InSAR) with two direction Referenced Linear Correlation (RLC) method was also used to localize the small deformation signal at the summit of Mount Sinabung by excluding the atmospheric phase delayed (Saepuloh *et al*., 2013). Time series observations based on InSAR were widely used to monitor active volcanoes, *e.g*. at Kilauea Volcano in Hawaii (Rosen *et al*., 1996), Etna Volcano in Italy (Lanari *et al*., 2007), Augustine Volcano in Alaska (Lee *et al*., 2007), Merapi Volcano in Indonesia (Saepuloh *et al*., 2010), Santorini Volcano (Papageorgiou *et al*., 2012), and Sinabung Volcano (Chaussard and Amelung, 2012; González *et al*., 2015). Volcano-related deformation is one of observation parameters accompanying seismicity in general. This study demonstrated an improvement of atmospheric phase delay removal from D-InSAR deformation signal using modified Referenced Linear Correlation (RLC) method (Saepuloh *et al*., 2013).

To observe syn-eruption impact to the environment, the dielectric constant and moisture content were also calculated in a series of ground surface using Sentinel-1A data. The following semi-empiric inversion model (Dubois *et al*., 1995) was applied to extract the dielectric constant of the surface. Then, the surface moisture was estimated following Topp model (Topp *et al*., 1980). Detailed description about dielectric constant extraction and surface moisture estimation was explained in next section.

Mount Sinabung in Karo Regency, North Sumatra Province, Indonesia, was selected as the studied area (Figure 1). Mount Sinabung is a stratovolcano type with the elevation of 2,460 m asl. The early activity of Mount Sinabung was presented visually by exposing ashes to the atmosphere at August 28th, 2010 and followed by pyroclastic flows at September 7th, 2010, after a prolonged repose interval. The eruptions increased the alert level to maximum and changed the cat-

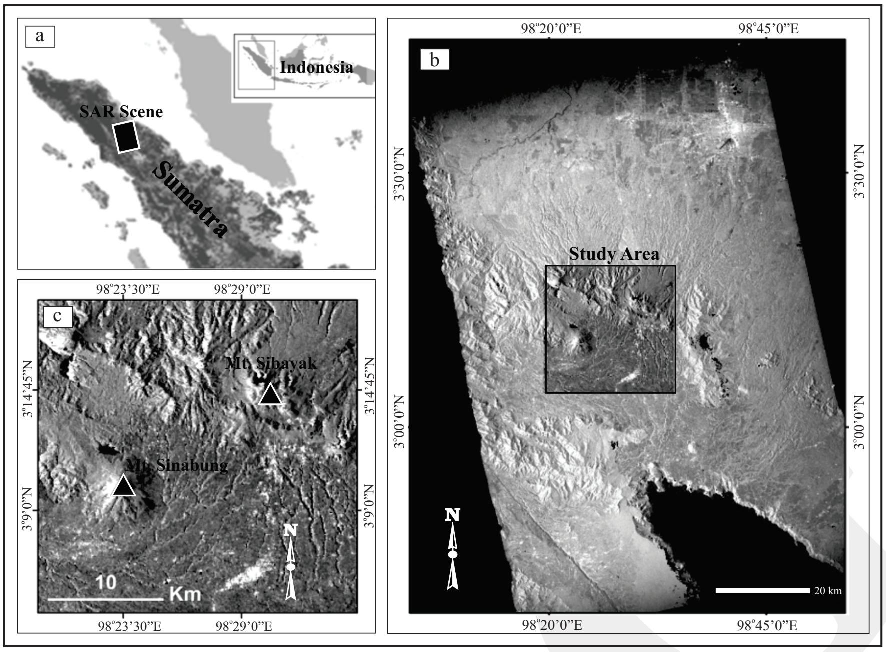

Figure 1. Studied area presented by ALOS PALSAR footprint in Sumatra Island (a), backscattering intensity image (b), subset of the SAR intensity image including Mounts Sinabung and Sibayak in black triangles (c).

egory "B" to "A" type volcano in the Indonesian volcanic rank. Mount Sibayak at 14 km NE of Mount Sinabung was also selected with the elevation of 2,094 m asl. as a reference for predicted unchange surface at a dormant volcano (Figure 1).

Data Collection and Methods

Data Collection

Twenty-one and nine scenes of the Phased Array type L-band Synthetic Aperture Radar (PALSAR) data on board the Advanced Land Observing Satellite (ALOS) and Sentinel-1A data were used, respectively. Detailed data used in this study were listed in Table 1. The ALOS PALSAR data were processed for lava dome roughness-changes detection and D-InSAR deformation due to L-band sensitivity for geomorphologic and structural feature detection (Saepuloh *et al.*, 2012). The Sentinel-1A in C-band frequency was also used to estimate the changes in surface moisture following the dielectric constant extraction. The level 1 Ground Range Detected (GRD) data from Interferometric Wide Swath (IWS) acquisition were processed using an open source Sentinel Application Platform (SNAP) programme. The C-band frequency is superior to estimate soil and vegetation moisture content in bare and vegetated areas (De Roo *et al.*, 2001; Zribi and Dechambre, 2003).

Lava Dome Roughness-Change Detection

Quantifying and modeling surface roughness at field using SAR data are a complicated problem because of topographic complexity, such as Root Mean Square (RMS) height, RMS slope, and correlation length (Campbell and Garvin, 1993) and also unknown radar parameters such as relative dielectric permittivity and relative magnetic permeability (Saepuloh *et al.*, 2015a). To simplify the radar equation, time series of SAR backscattering intensity images were used at a fixed point of the summit lava dome. Therefore, the unknown parameters could be excluded due to the absent of new volcanic products extruded prior to the eruption (Saepuloh *et al.*, 2013). Reasoning and estimation of lava dome roughness changes were explained as follows.

The SAR backscattering coefficient σ^0 is a power return to the receiver sensor as a function of several parameters and explicitly could be

Table 1. SAR Data Used in this Study from ALOS PALSAR And Sentinel-1A

No	Scene ID	Date	Sensor	Polarization Mode
1	PASL10C0702201611471206080041	2007/02/20	ALOS PALSAR	HH
2	PASL10C0707081611471206080042	2007/07/08	ALOS PALSAR	HH+HV
3	PASL10C0708231611401206080044	2007/08/23	ALOS PALSAR	HH+HV
4	PASL10C0801081610411206080047	2008/01/08	ALOS PALSAR	HH
5	PASL10C0802231610061206080043	2008/02/23	ALOS PALSAR	HH
6	PASL10C0804091609231206080049	2008/04/09	ALOS PALSAR	HH
7	PASL10C0805251608341206080051	2008/05/25	ALOS PALSAR	HH+HV
8	PASL10C0810101609551206080045	2008/10/10	ALOS PALSAR	HH+HV
9	PASL10C0811251610441206080046	2008/11/25	ALOS PALSAR	HH
10	PASL10C0901101611261206080050	2009/01/10	ALOS PALSAR	HH
11	PASL10C0902251612021206080048	2009/02/25	ALOS PALSAR	HH
12	PASL10C0907131613061206080053	2009/07/13	ALOS PALSAR	HH+HV
13	PASL10C0908281613201206080052	2009/08/28	ALOS PALSAR	HH+HV
14	PASL10C0911281613301206080063	2009/11/28	ALOS PALSAR	HH
15	PASL10C1001131613271206080054	2010/01/13	ALOS PALSAR	HH
16	PASL10C1002281613141206080065	2010/02/28	ALOS PALSAR	HH
17	PASL10C1007161611581206080066	2010/07/16	ALOS PALSAR	HH+HV
18	PASL10C1008311611251206080069	2010/08/31	ALOS PALSAR	HH
19	PASL10C1010160160461206080064	2010/10/16	ALOS PALSAR	HH+HV
20	PASL10C1012011610011206080067	2010/12/1	ALOS PALSAR	HH+HV
21	PASL10C1101161609091206080068	2011/01/16	ALOS PALSAR	HH
22	S1A_IW_GRDH_1SDV_20150218T231128	2015/02/19	SENTINEL-1A	VH+VV
23	S1A_IW_GRDH_1SDV_20150513T231130	2015/05/14	SENTINEL-1A	VH+VV
24	S1A_IW_GRDH_1SDV_20150606T231133	2015/06/07	SENTINEL-1A	VH+VV
25	S1A_IW_GRDH_1SDV_20150630T231157	2015/07/01	SENTINEL-1A	VH+VV
26	S1A_IW_GRDH_1SDV_20150724T231158	2015/07/25	SENTINEL-1A	VH+VV
27	S1A_IW_GRDH_1SDV_20151215T231154	2015/12/16	SENTINEL-1A	VH+VV
28	S1A_IW_GRDH_1SDV_20160108T231153	2016/01/09	SENTINEL-1A	VH+VV
29	S1A_IW_GRDH_1SDV_20160201T231152	2016/02/02	SENTINEL-1A	VH+VV
30	S1A_IW_GRDH_1SDV_20160225T231152	2016/02/26	SENTINEL-1A	VH+VV

written as follows:

$$\sigma^0 = (4k^4 h_0^2 cos^4\theta_i)|\alpha|^2\omega \text{ ....(1)}$$

Where:

k : is the wave number,

h_0 : is the surface roughness,

θ_i : is the angle of incidence from the mean normal direction to the surface,

α : is proportional to polarization state, and

ω : is roughness height spectral density of the surface topography.

For the case of SAR backscattering time series at a fixed point of the surface lava dome, the k, θ_i, α, and ω were predicted to be constant, because the path/row of data series, surface material, and topography are coherent. Therefore, only h_0 influences the σ^0. Figure 2 shows the illustration of lava dome roughness on SAR termed as drSAR for Showa-Shinzan lava dome growth (Schmincke, 2004). After the eruption period, the summit of the volcano is relatively flat and

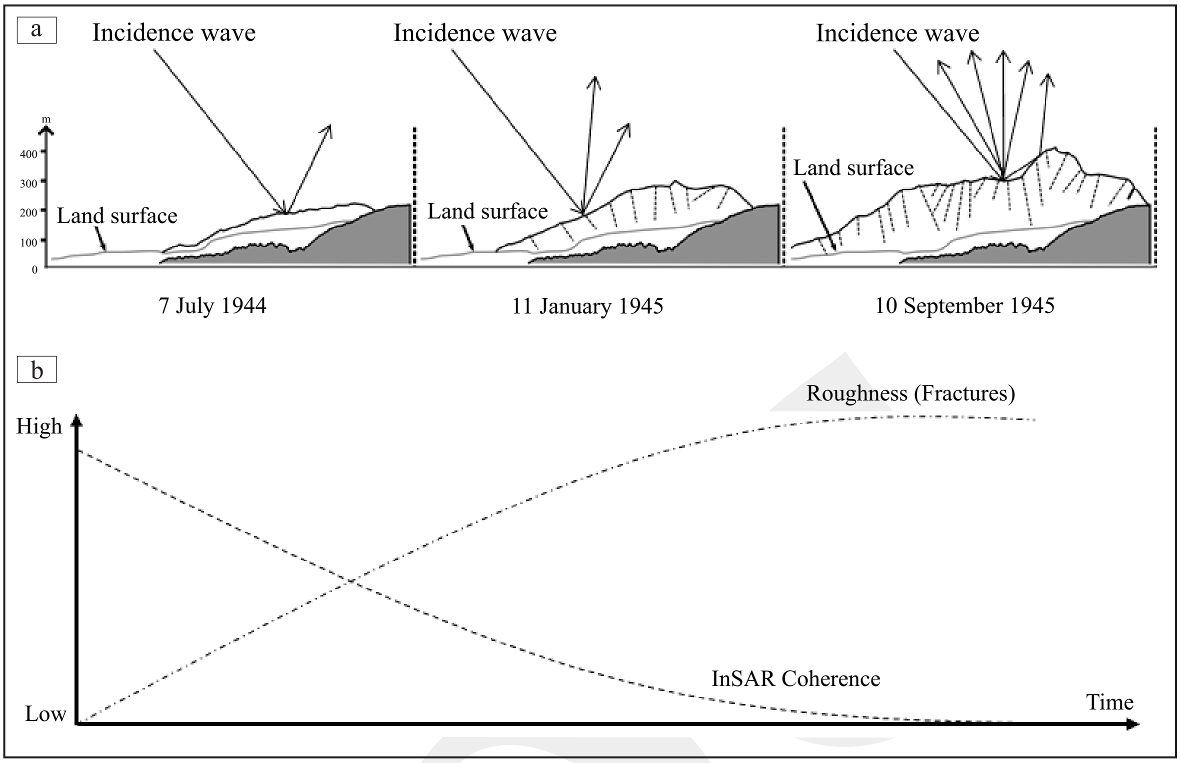

Figure 2. Illustration of Showa-Shinzan lava dome growth (modified from Schmincke, 2004) related to the increase of fracturing and surface roughness presented by high backscattering intensity signal.

produces low backscattering (Figure 2a). When the lava dome is growing, its volume increases and produces fracturing system at the surface. The fractures produce rough surfaces which are presented by higher backscattering intensity than flat surface (Figure 2b). Therefore, the maximum surface roughness will be achieved prior to the eruption. After the eruption, the drSAR might be affected not only by fractures at surface lava dome, but also by new volcanic products.

For drSAR processing, firstly the ALOS PALSAR level 1.5 intensity images were geocoded to transform the location of each image pixel from slant to the ground range coordinate. Then, co-registration among the images was also applied to assure the correctness of pixel location followed by subsetting image around the summit. The purpose of subsetting process is to simplify the detection process and to reduce the time processing. Finally, a layer-stacking process was performed to the sixteen images. Selecting Region of Interest (ROI) 3×3 pixels (=90×90 m) at the summit of Mounts Sinabung and Sibayak were performed to observe surficial changes related to volcanic activity. The size of ROI was selected due to detectability of a new volcanic product under ALOS PALSAR intensity image 30 m resolution (Saepuloh *et al.*, 2013). The processing illustration was depicted in Figure 3. The drSAR change detections were applied based seed-fill method with pixel growth criterion (Saepuloh *et al.*, 2013). The centre point of the lava dome was used to quantify the area of drSAR at the summit of Mount Sinabung.

Modified Referenced Linear Correlation of D-InSAR Deformations

The atmospheric conditions might influence the measured ground range and cause phase delay propagation (Papageorgiou *et al.*, 2012). Several techniques have been developed to reduce the atmospheric effects, such as integration with Weather Research and Forecast (WRF) model based on MODIS data (Gong *et al.*, 2011), Pairwise Logic (Hanssen, 2001), Referenced Linear Correlation (Saepuloh *et al.*, 2013), PS-InSAR technique (Massonnet and Feigl, 1998; Sousa

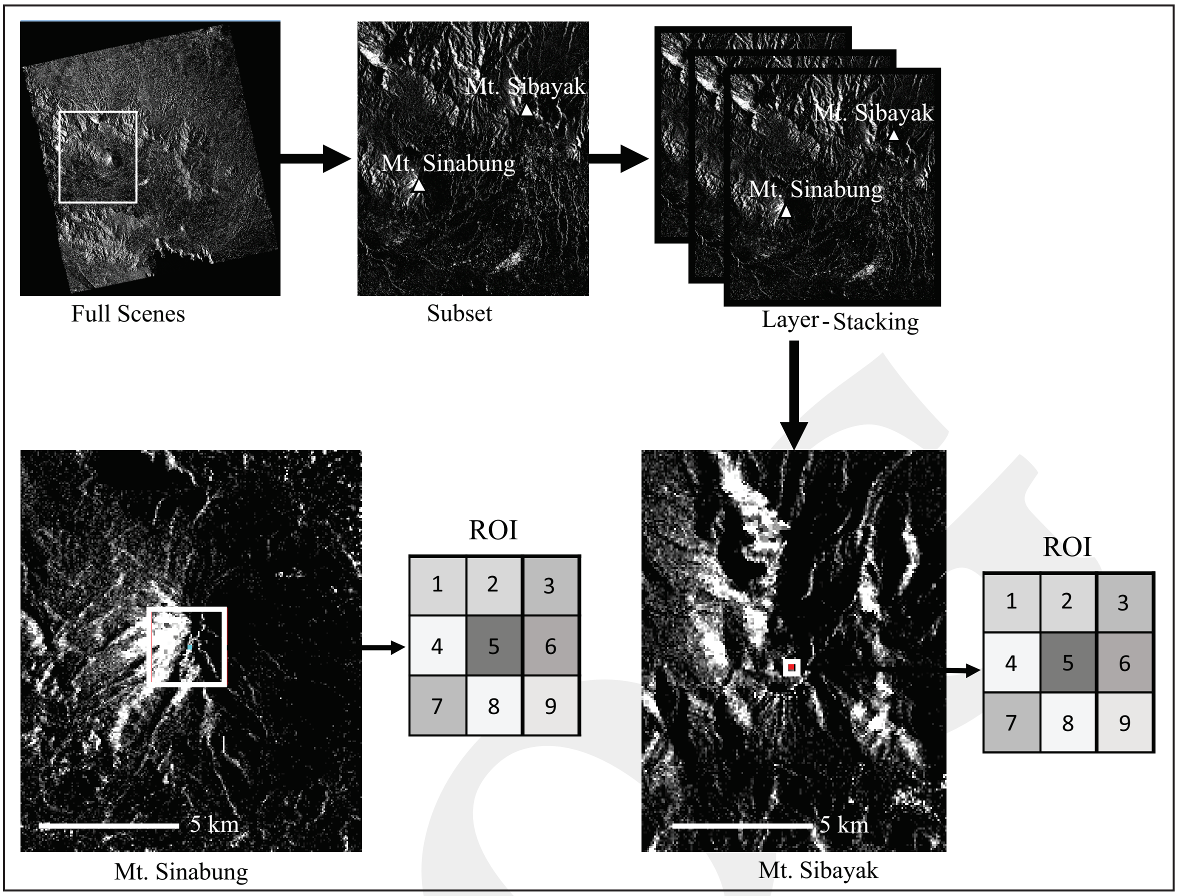

Figure 3. Image stacking and selection of ROI (Region of Interest) by pixel labeling at the summit of Mount Sinabung and Mount Sibayak.

et al., 2010), stacking method and integration between GPS and MODIS data (Li *et al*., 2009, 2005). Selecting the appropriate technique in mitigating the atmospheric artifact depends on the availability of SAR data scenes, the method used for InSAR processing, the atmospheric condition, and the availability of external data. In this study, a high applicability technique was proposed under the tropical zone to reduce atmospheric artifact in the interferogram phase using modified Referenced Linear Correlation (mRLC). This technique requires pair-wised interferogram and the Digital Elevation Model (DEM) or high-resolution topographical map. The pair-wise logic was used to generate interferogram by reducing the atmospheric phase delay of common paired D-InSAR data (Hanssen, 2001).

The modification was taken into account from previous work (Saepuloh *et al*., 2013) using correlation between topographic elevation to deformation along range (north-south) and azimuth directions (west-east). The reference location was selected at the nearest volcano without significant eruptive activity signals at the summit. Mount Sibayak about 15 km NE of Mount Sinabung is the most appropriate candidate for the reference location in this study because of no eruptive signature at the summit although the earthquake swarm are still recorded in a depth of less than 30 km (Nugraha *et al*., 2018). The mRLC calculates the regression between elevation and deformation at Mount Sibayak in two directions and serves as a reference for background deformation originated from atmospheric phase delay. For each interferogram, the linear regression was calculated and the equation was used to extrapolate the atmospheric phase model spatially as presented in Figure 4. Subtracting the atmospheric phase model from the pair-wise interferogram produced a final deformation signal in the interferogram.

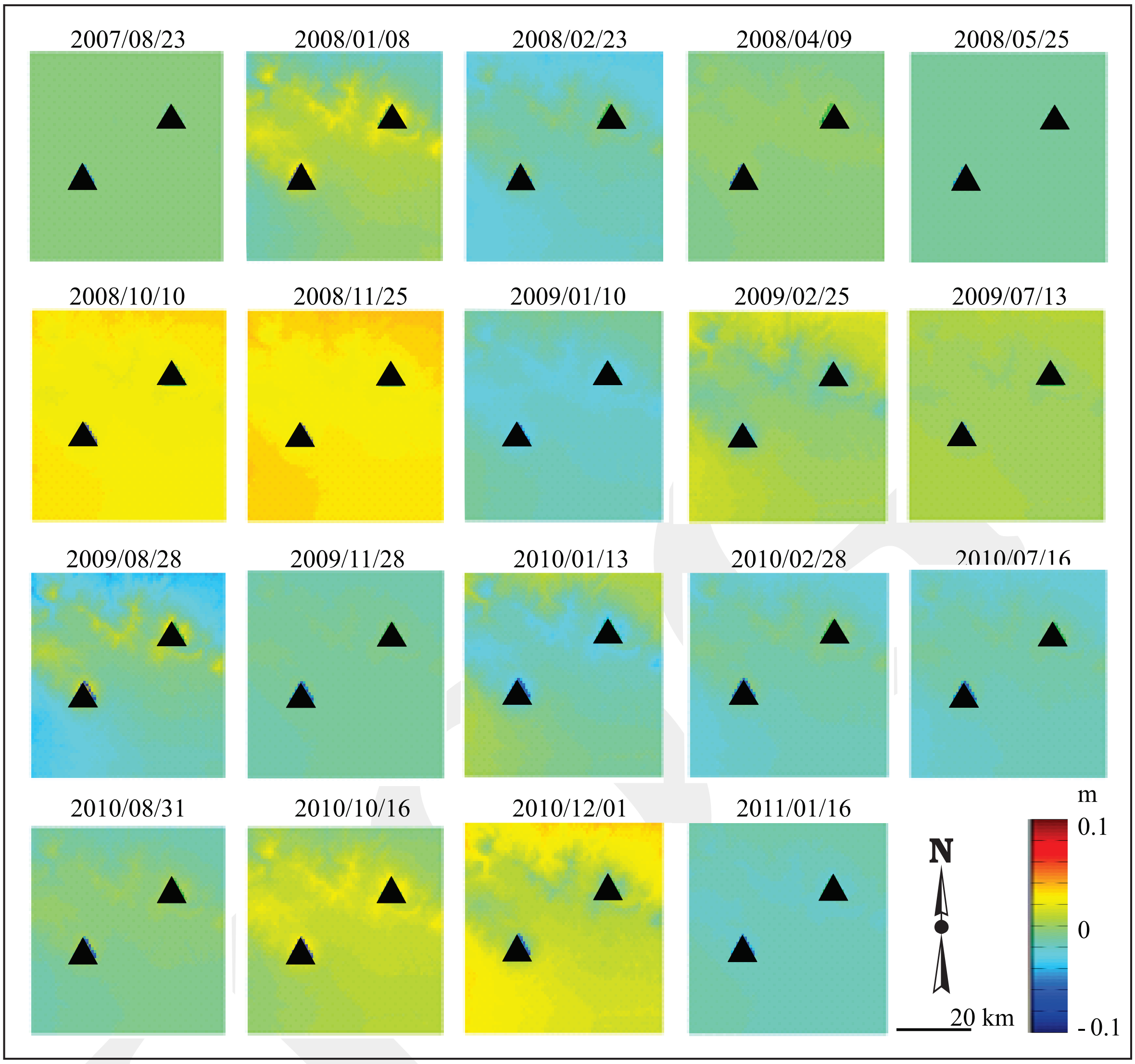

Figure 4. Atmospheric phase model calculated based on mRLC for each pair-wised D-InSAR with YYYY/MM/DD date format, the triangle on the west and east parts are Mounts Sinabung and Sibayak, respectively.

Surface Moisture Estimation Using Sentinel-1A Data

Sentinel-1A Ground Range Detected (GRD) high resolution data was used to estimate surface moisture of land cover at and around Mount Sinabung following the eruption. The GRD data were focused, multilooked, and projected to ground range using an earth ellipsoid model. The backscattering coefficient of GRD data σ^0_{db} was then calculated as follows:

$$\sigma^0{}_{db} = 10\log_{10}\frac{(DN)}{A_\sigma^2} \quad \text{.......................(2)}$$

where *DN* and A_σ^2 are digital number of SAR amplitude and look up table for transforming radar reflectivity to cross-section in ground range plane, respectively.

A terrain correction process was also applied by selecting twenty-five Ground Control Points (GCPs) with RMSE 0.2 pixel to obtain the accurate geometric position of the σ^0_{db} image in geographic coordinate. Then, the σ^0_{db} images were filtered using Lee filter to enhance land cover contrast, especially for the agriculture area (Ozdarici and Akyurek, 2010). The Lee filter was selected, because the studied area was mostly covered by agriculture. To estimate surface moisture, parameter influence to σ^0_{db} was firstly calculated including surface roughness h_0 and dielectric constant ε of the surface (Gharechelou *et al.*, 2015). The h_0

is variance of earth surface elevations above the horizontal line quantified by Root Mean Square (RMS) height (Saepuloh *et al.*, 2015a). Series of field measurement were used to obtain the h_0 from the σ^0_{db} the following images (Saepuloh *et al.*, 2012; Witra *et al.*, 2017). The h_0 derived from the σ^0_{db} could be calculated as follows:

$$h_0 = \lambda\sqrt{-\frac{1}{60}\ln\left(1-\frac{10^{(0.1\times\sigma^0_{db})}}{0.04\cos\theta_i}\right)} \quad \text{................(3)}$$

Where:

λ : is the wavelength used by Sentinel-1A sensor (=5.6 cm).

Then, following Dubois model (Dubois *et al.*, 1995), the ε was calculated as follows:

$$\varepsilon = \frac{log_{10}\dfrac{10^{2.35}\sigma^o_{db}\times(sin\,\theta_i)^3}{((kh_0\ sin\,\theta_i)^{1.1}\,\lambda^{0.7})\times(cos\,\theta_i)^3}}{0.46\,tan\,\theta_i} \quad \text{...(4)}$$

The surface moisture was inverted from the ε (equation 3) following Topp model (Topp *et al.*, 1980). This model is effective for retrieving soil moisture (Das and Paul, 2015; Song *et al.*, 2010) and could be calculated as follows:

$$M_v = (-5.3\times10^{-2}) + (2.92\times10^{-2}\varepsilon) - (5.5\times10^{-4}\varepsilon^2) + (4.3\times10^{-6}\varepsilon^3) \quad \text{.....(5)}$$

Where:

M_v : is the volumetric moisture content or the amount of stored water in surface materials.

Results

Small Signature of an Eruption Precursor

To obtain the surface changes at the summit, the area size of the drSAR termed as D-Zones was calculated for 16 ALOS PALSAR data series in 2007–2010. The D-Zones at the summit of Mount Sinabung was presented by red portion in backscattering intensity images of ALOS PALSAR (Figure 5). Since the same incidence angle of ALOS PALSAR data was used, the detected D-Zones presented the physical property of lava dome surface such as dielectric and surface roughness parameter. The persistent pixel location was selected to observe the changes over time. Therefore, the influence of surface roughness is

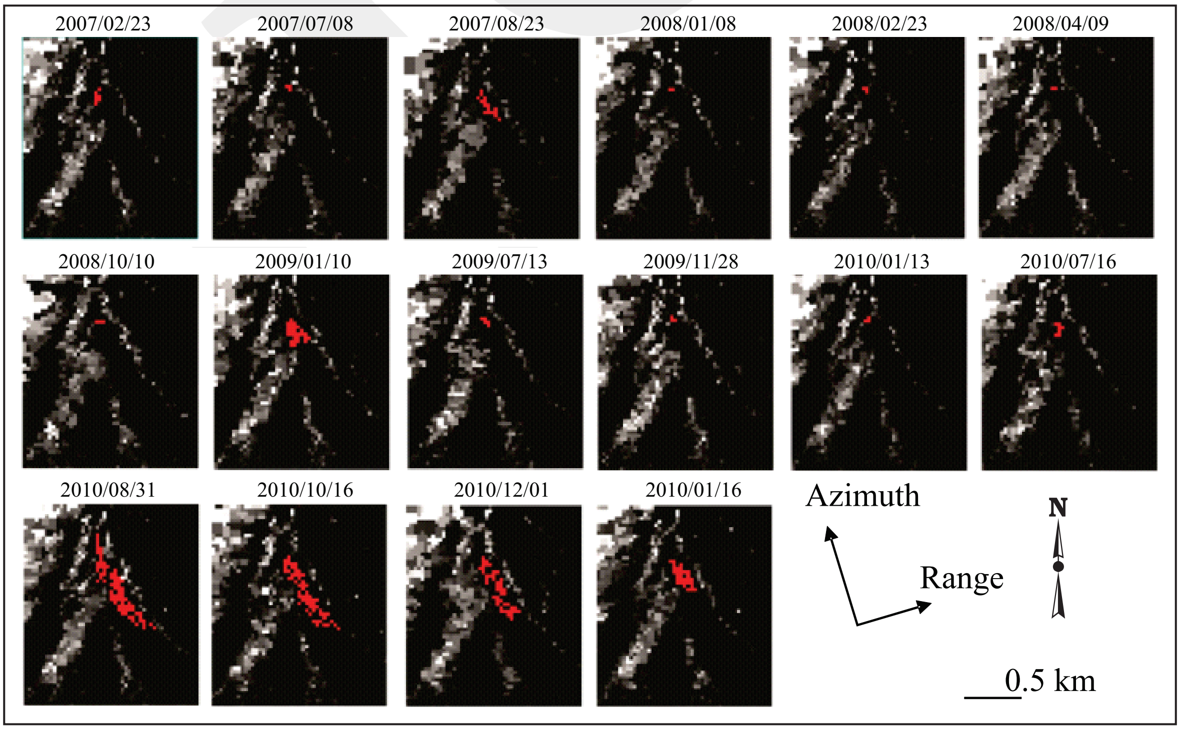

Figure 5. D-Zones at the summit of Mount Sinabung were presented by red portions.

presumed stronger than dielectric constant. When the magma ascends to the shallow reservoir, the dielectric property of lava dome will be constant, but its surface roughness might be increased as explained in previous section.

The D-Zones were located mostly at the centre of the summit prior to the eruption at August 28th, 2010. The small surface change of the D-Zones was detected relatively toward SE from the centre of the summit at August 23rd, 2007 and January 10th, 2009. Then, the large surface changes following the first eruption were detected at August 31st, October 16th, and December 1st, 2010. The SE direction is the most vulnerable zones to the distribution of volcanic products.

In addition to the surface change of the D-Zones, the surface deformation using D-InSAR after mRLC atmospheric correction was presented as explained in previous section. Time series D-InSAR deformation were presented by blue and red for deflation and inflation, respectively (Figure 6). The deformations at the summit of Mounts Sinabung and Sibayak were focused by excluding the other deformation possibility out of the two summits (black triangles).

The performance of mRLC is depicted by the initial and corrected deformation at the summit of Mounts Sinabung and Sibayak (Figure 7). Their initial interferogram showed large variation of deformation about -0.03 to 0.03 m and -0.03 to

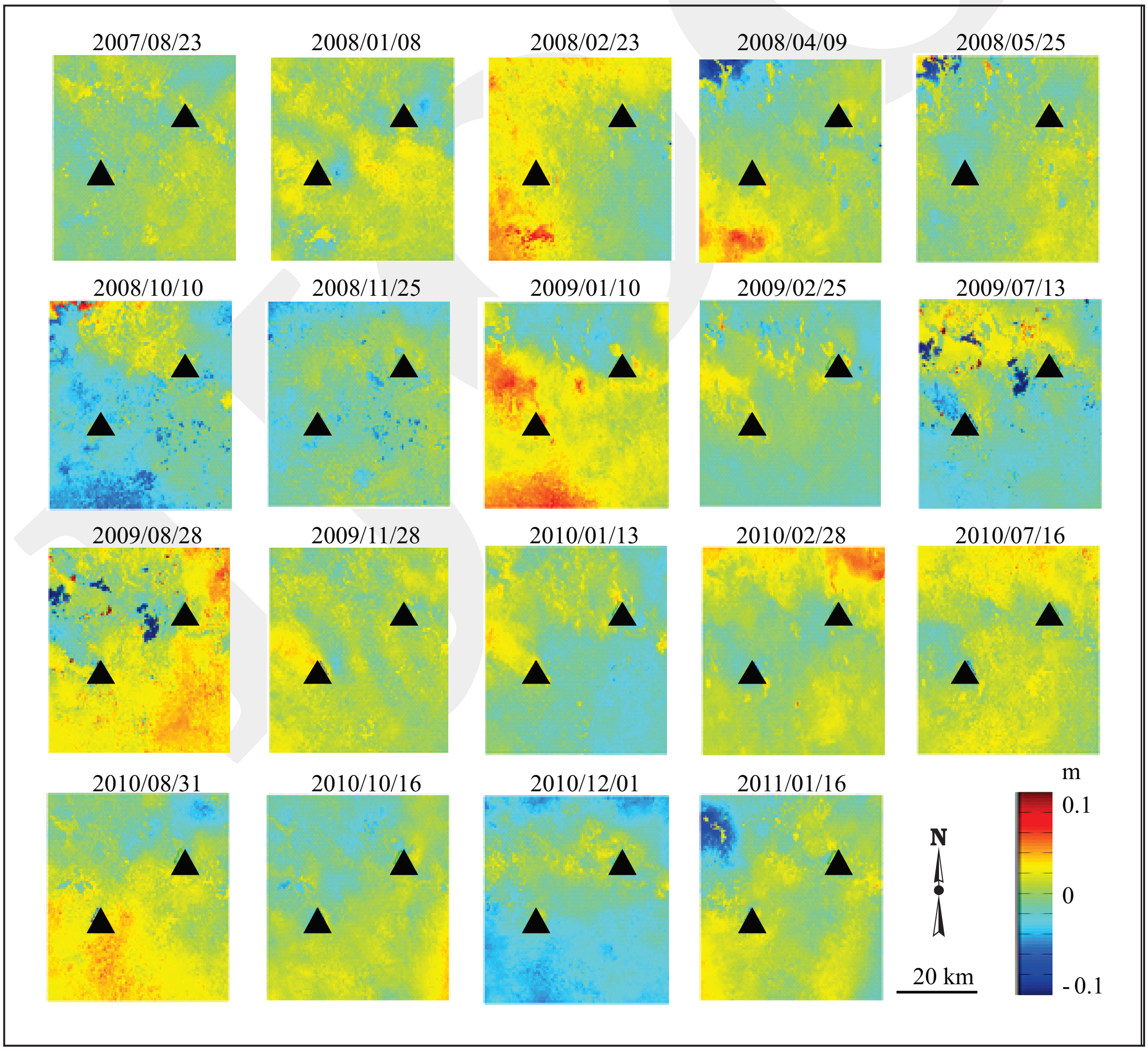

Figure 6. Observed ground deformations after mRLC atmospheric correction in meter units for each pair-wised D-InSAR with YYYY/MM/DD date format. The triangle on the west and east parts are Mounts Sinabung and Sibayak, respectively.

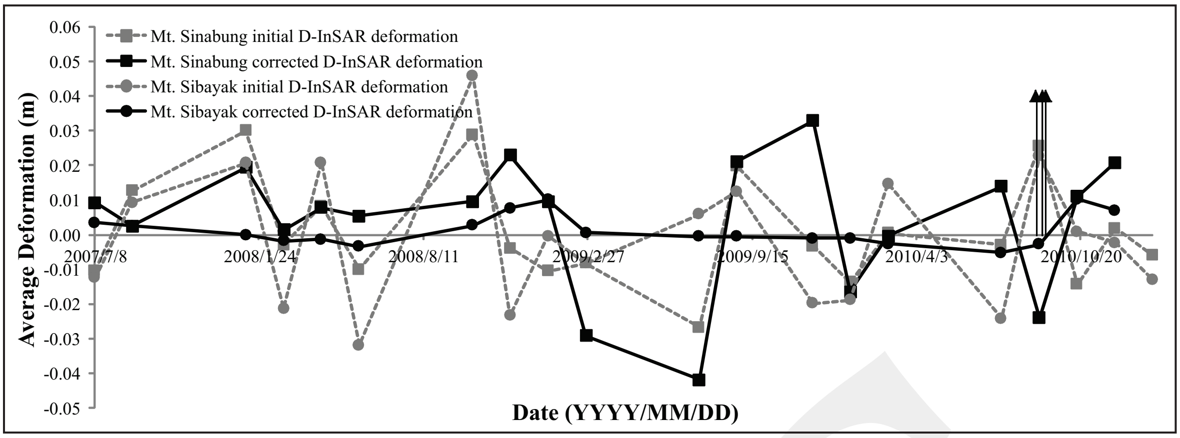

Figure 7. D-InSAR deformation time series prior to the Mount Sinabung eruptions on August 27th, September 3rd, and September 4th, 2010 presented by black arrows showing that the atmospheric signal still influences the detected deformation (dashed lines). Mount Sibayak was used as a background deformation by the mRLC atmospheric correction and the average deformation was calculated by 3×3 pixels at the summit of Mounts Sinabung and Sibayak presented by subset Figure 2.

0.06 m with Root Mean Square (RMS) 0.015 and 0.019, respectively. The large variation of deformation was predicted from the atmospheric phase delay influenced to the interferogram. In contrast, the corrected interferograms at Mount Sibayak were presented by almost 0 m deformation with RMS 0.004 m. The mRLC reduced about 27% noise from deformation phase signal. For Mount Sinabung, the large variations of deformation related to atmospheric phased delay were reduced and the deformation signal was improved from the initial interferogram with RMS 0.018 m. The initial eruptions at Mount Sinabung are overlaid in the deformation plot by black arrow in Figure 7.

Current Eruption Impacts to Ground Surface

Obtaining the impact of the eruptions to the land cover, the distribution of volcanic products and modeled surface moisture around Mount Sinabung was analyzed using Sentinel-1A as explained in previous section. The visual comparison between the eruption periods in 2015 and 2016 was used based on colour composite of polarimetric mode R, G, B for VH, VV, VH (Figures 8a and b). The selected colour composite was advantageous to enhance the surface parameter related to surface roughness and electrical property influenced strongly to the cross-polarization VH and co-polarization VV, respectively (Saepuloh *et al.*, 2015a; Saepuloh *et al.,* 2015c). The red

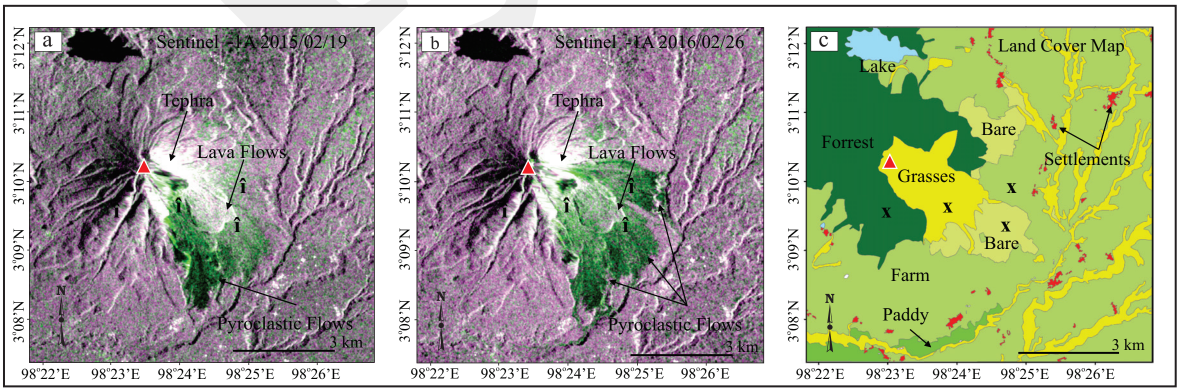

Figure 8. Colour composite of Senitinel-1A backscattering intensity images for R, G, B=VH, VV, VH at 2015/02/19 (a) and 2016/02/26 (b) showing the distribution of volcanic products after eruptions in 2015, and land cover types (c) at Mount Sinabung (BKSPN, 2009).

portions in the composite colour indicated the volume scattering from vegetation covers at the old volcanic formation with intensive erosional structures. The red portions with a radial pattern from the summit of Mount Sinabung were distribution of lava and pyroclastic flow deposits. The green portions toward the E and SE from the summit were interpreted as the new volcanic products including tephra, pyroclastics, and lava flows. The variety of electrical properties such as opened ground surface distinguished the appearance of volcanic products.

The volcanic products produced by the eruptions devastated land cover, especially at E−SE (Figure 8c). The grasses, bare land, farm land, paddy field, and settlements were affected mainly by pyroclastic flow deposits. The temporal analyses were pointed at "×" symbols at the forest, bare, and farm land based on published land cover map (BKSPN, 2009).

The time series of volcanic products influencing the land cover were presented by the changes of surface moisture from February 19th, 2015 to February 26th, 2016 (Figure 9). The low surface moisture presented by red portion is concordant with the distribution of lava flow deposits and the high surface moisture presented by blue portion is concordant with the distribution of pyroclastic flow deposits. The low surface moisture at the western flank from the summit was interpreted from the tephra deposits as well as the influence of the back slope effect from west Line of Sight (LOS). The pores of fragmental material from pyroclastics and tephra served as the infiltration media from meteoric water to the ground. Therefore, the surface moisture is high at their distribution. In contrast, the presence of fewer pores at lava flow deposits than pyroclastic and tephra causes the surface moisture is low at their distribution. The variation of surface moisture in temporal and spatial distribution is targeted as the effect of the eruptions to the land cover type as explained in the following section.

Interpretation and discussion

The area size of lava dome roughness or D-Zone extracted based on drSAR at Mount Sinabung was observed to change prior to the eruptions (Figure 10). In spite of low variation curve, the small changes were detected in 2007 and 2008 followed by constant trend in 2009. Then, the increment was noticeable in January to August 2010. The high D-Zone was detected prior to the eruption at July 16th, 2010 about 5,121 m^2. The maximum D-Zone size was detected four days after the eruption at August 31st, 2010

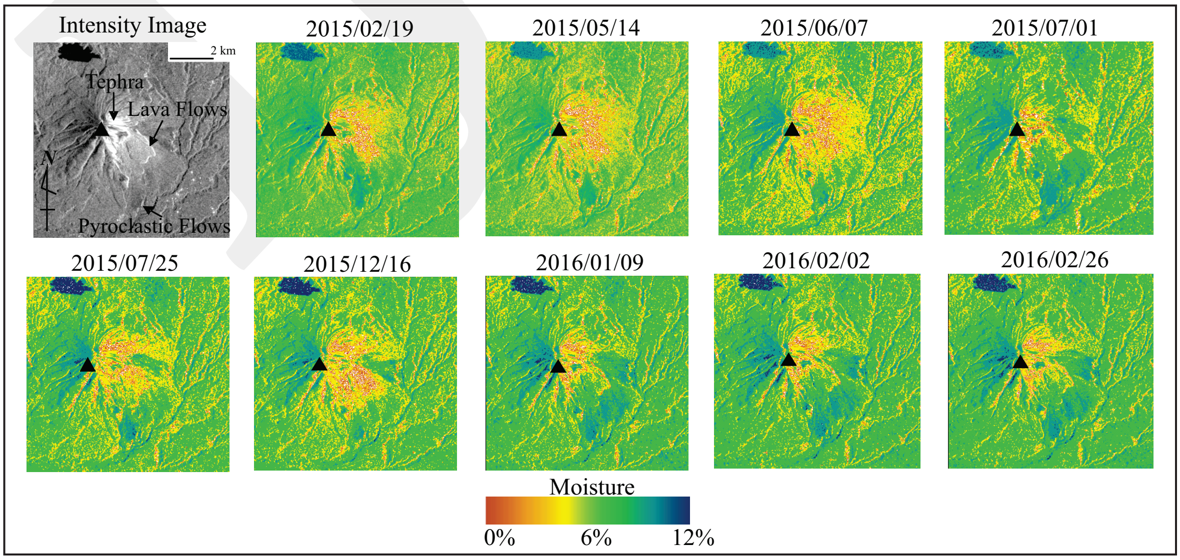

Figure 9. Time series of surface moisture extracted using Dubois model from Sentinel-1A SAR data shows ground surface changes related to new volcanic products.

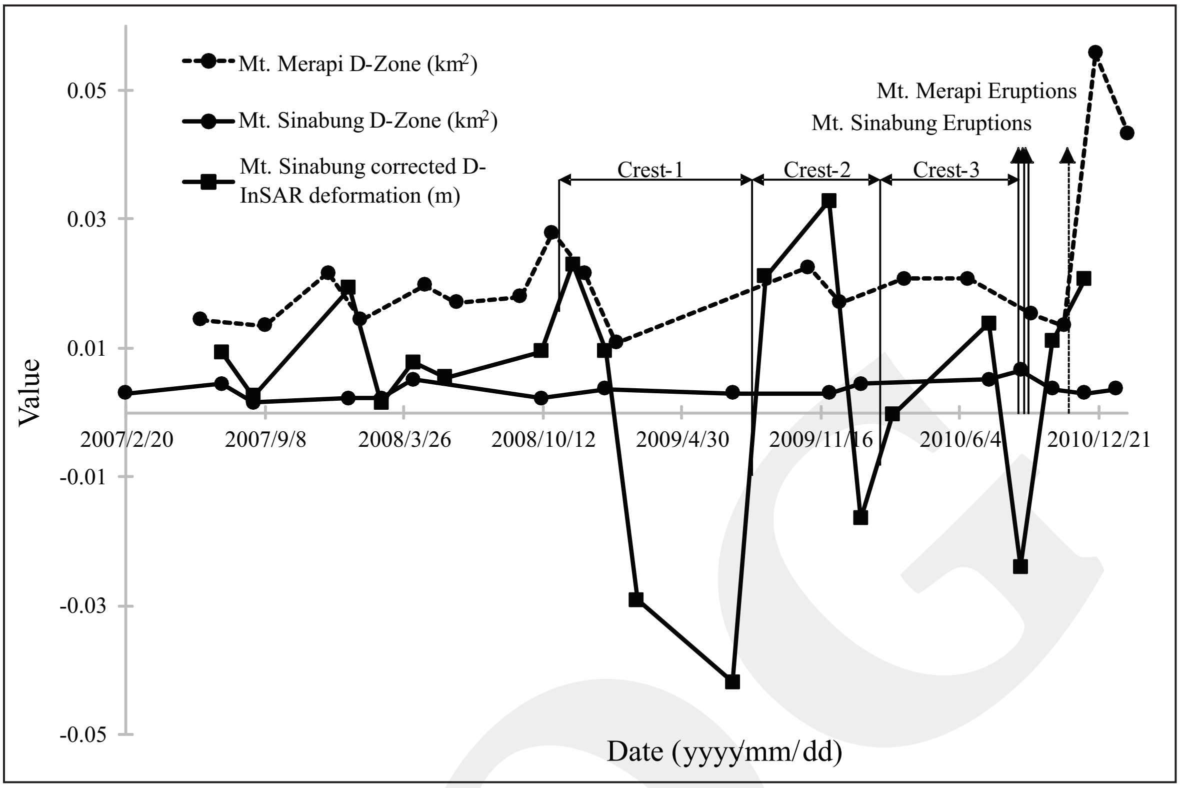

Figure 10. Time series of D-Zone and D-InSAR deformation at the summit of Mount Sinabung with background D-Zone at Mount Merapi prior to the eruption periods. Black and dashed lines are eruption periods of Mounts Sinabung and Merapi, respectively.

about 6,584 m^2. The D-Zone prior to the eruption was interpreted to be affected mainly by surface roughness originated from fracturing system at lava dome, and after the eruption the D-Zone was affected also by the roughness of new volcanic products. The increment of the D-zone prior to the eruption could be explained also by the imaging of seismic tomography from October 2010 to July 2013 (Indrastuti *et al*., 2019). The low anomaly seismic velocity was reported in a shallow depth at west-southwest from the summit and associated with saturated crack density that high pressurized hydrothermal fluids release to the summit produced the phreatic eruption. Accordingly, it may be possible that the pressure source of the phreatic eruption originated from the west−southwest so that the new volcanic products were detected toward to east-southeast from the summit as presented in this study.

To confirm the change pattern, the case of Mount Merapi eruption on November 2010 was used as depicted by dashed-dot curve (Figure 10). The large variation was detected at the summit lava dome of Mount Merapi in 2007–2008. In 2010, the D-Zones decreased about 13,500 m^2 and followed by a maximum increase in December 17th, 2010 about 55,800 m^2. In contrast to Mount Sinabung, the eruption of Mount Merapi is characterized by the decrease of D-Zone prior to the eruption. The different eruption type between magmatic eruption at Mount Merapi and phreatic eruption at Mount Sinabung might be affected the surface lava dome as detected by drSAR. The interaction between water and magma for phreatic eruption produces a high pressure beneath the surface and fracturing system at lava dome surface (Saepuloh *et al*., 2015b).

Analyzing the D-Zone changes over time in the view point of deformation; the D-InSAR deformation series following mRLC atmospheric correction at Mount Sinabung was analyzed. The D-InSAR deformation and D-Zone size were compared to the Mount Merapi eruption in 2010 to characterize a different eruption style (Figure

10). The first significant inflation was detected on November 2008 about 2.3 cm and followed by the high deflation about 4.2 cm on July 2009 termed as Crest-1. The second significant inflation was reached on November 2009 about 3.3 cm. That inflation followed by a deflation until January 2010 about 1.7 cm is termed as Crest-2. The third significant inflation occurring on July 2010 about 1.4 cm was followed by a phreatic eruption at August 28th, 2010 termed as Crest-3. Then, the summit of Mount Sinabung began to deflate until August 31st, 2010 about 2.4 cm. The only GPS measurement in 2012-2013 confirms that the horizontal displacement from the summit flanks occurring in 2012-2013 is in centimeter scale (Kriswati *et al*., 2015). Therefore, a low rate deformation about centimeter scale detected by D-InSAR and GPS as well as enlargement of D-Zones indicates that the small amount of magma batches had been feeding the shallow reservoir continuously. High magma viscosity with a large amount of supply is predicted to the low rate deformation as presented in this study.

The three inflation-deflation periods, detected on November 2008 to August 2010, are interpreted as signatures of magmatic plumbing system from the crust and/or deep magma reservoir about 5.2 - 8.7 km depth from the summit (Nugraha *et al*., 2017). The migration process of magma batches and dike generations through the subsurface will reach a neutral buoyancy level, at which the dike will cease vertical ascent, but continue to propagate laterally and widen (Wyrick and Smart, 2009). Widening dike will allow a graben-like to form which was indicated by the deflation at ground surface (Mastin and Pollard, 1988). The limited seismicity data before the eruption caused difficulty for a deep analysis, *e.g*. before and during the phreatic eruption. Following the eruptions, the frequency of shallow volcanic earthquakes increased from eleven to forty-nine times per day at September 4th, 2010, and deep volcanic earthquakes increased from fifteen to thirty-six earthquakes per day between September 4th and 5th, 2010 (Iguchi *et al*., 2011). These conditions illustrated that the transport system connected the deep to shallow reservoir through a conduit. The magma has been stored in the shallow reservoir and followed by crystallization and degassing processes which caused the inflation at ground surface prior to the eruption (Bodnar *et al*., 2007). Then, the deflation occurred following the first eruption due to withdrawal magma pressure that fed the eruption (Lu *et al*., 2005). The crystallization process transformed magmatic fluid to partly solid crystals caused decreasing volume, but increased the pressure due to degassing process. Therefore, the pressure increased significantly in the shallow reservoir prior to the later magmatic eruption in 2013. Decreasing volume due to crystallization as well as magma migration and dike generation might cause prior deflation to an eruption as also recorded in the case of Mount Merapi eruptions 2010 (Saepuloh *et al*., 2013), Mount Hekla 1991 (Sigmundsson *et al*., 1992), and Mount Krafla 1978 (Einarsson and Brandsdottir, 1978).

Following the phreatic eruption in 2010, the magmatic eruptions have been initiated at September 15th, 2013 and continued until recently (Gunawan *et al*., 2017; Nakada *et al*., 2017). A new phase of Mount Sinabung eruptions has forced people around the volcano to evacuate from the hazardous zones. The long eruption phase has been started and characterized by raised ash plumes about 2 km above the summit and generation of pyroclastic flows and lava (Gunawan *et al*., 2017). Observing the syn-eruption impact to the ground surface, the surface moisture change using Sentinel-1A data was analyzed following the explained method in previous section. There are four land cover types affected by volcanic products. Thus, four locations presented by "×" symbols were selected as points of interest (Figure 8). The volcanic products supplied sulphur, selenium, potassium, and magnesium, and influenced the ground surface composition (Cronin *et al*., 1998). Surface moisture, as well as the above mentioned minerals, is one of the basic elements for soil fertility (Box *et al*., 1963). Analyzing the temporal change of surface moisture related to exposed volcanic products was discussed as follows.

Fragmental and pores volcanic products such as pyroclastics and tephra served space for meteoric water to hold, so that surface moisture might increase in the affected area. Interestingly, based on the result, the surface moisture relatively decreases on the syn-eruption period. The temporal variation of surface moisture at four points of interest with the number of eruptions is depicted by Figure 11. Accordingly, the surface moisture pattern shows a similar trend among land cover types that the decrease surface moisture at June 14th, and December 16th, 2015 are followed by the increase in July 1st, 2015 and January 9th, 2016. The decrease of surface moisture could generally be identified following the eruptions, *e.g.* the low surface moisture at June 14th, 2015 after the eruptions on March-April 2015. The similar phenomenon is also noticed that the low surface moisture at December 16th, 2015 is detected following the series of eruptions on July to November 2015.

The new volcanic products such as hot pyroclastic and lava flows are interpreted to evaporate the water content at the surface. Evaporation of surface moisture content due to drying from hot temperature is a common case in decreasing surface moisture (Hirschi *et al*., 2011; Zampieri *et al*., 2009). Following the decrease, the surface moisture increases due to infiltration of meteoric water to the pores volcanic products such as pyroclastics and tephra as presented by a high surface moisture at July 1st, 2015 and January 9th, 2016. Another possibility of low surface moisture was due to the lowering precipitation rate around Mount Sinabung. The volcanic eruptions produced ashes to the atmosphere and decreased the precipitation rate such as at El Chichón and Mount Pinatubo 1991 (Trenberth and Dai, 2007). The large eruptions are concordant to the wide decrease in precipitation (Peng *et al*., 2010). Further field investigations and meteorological analyses are necessary and aimed to the next step in this study.

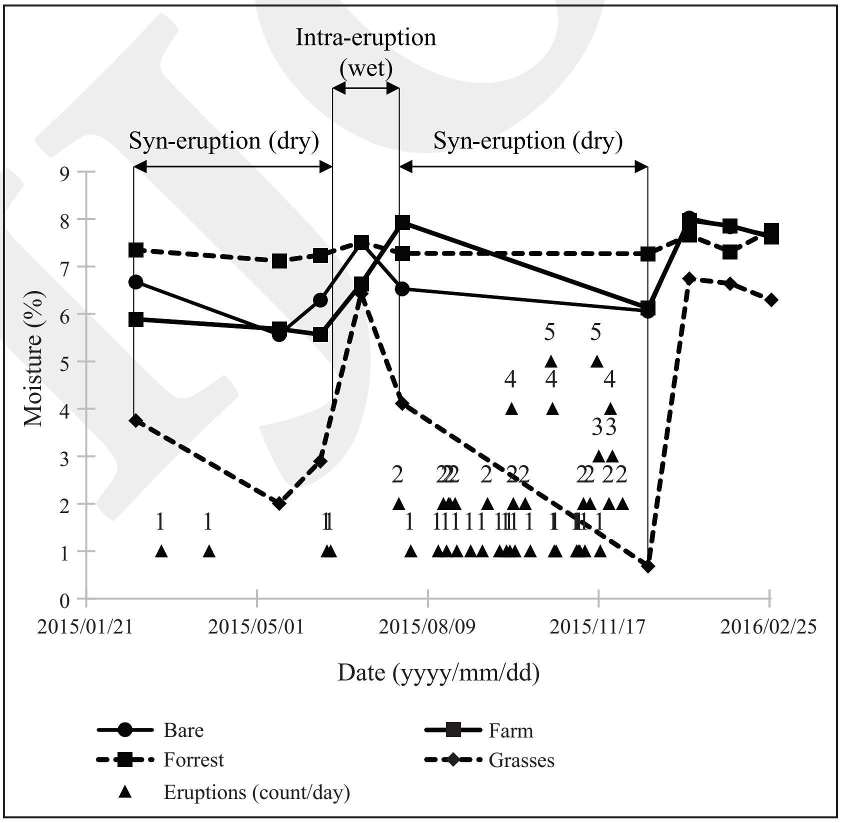

Figure 11. Time series detected surface moisture derived by Dubois model using Sentinel-1A SAR. The black triangles are the number of eruptions prolonged after the initial eruption in 2010.

Conclusion

The fracturing system of lava dome growth is explained responsible to detect rough surface and presented by a high backscattering intensity. The maximum D-Zone achieved prior to the eruption of Mount Sinabung at August 28th, 2010 was located mostly at the centre of the summit. Following the eruption, the increase of D-Zone was also affected by new volcanic products toward SE from the summit. The change of D-Zone prior to the eruption is concordant with corrected D-InSAR deformation using modified Referenced Linear Correlation (mRLC). The mRLC was proved about 27% effective to remove atmospheric phase delay from the initial interferogram presented by decreasing of RMS deformation variation at reference location from 0.015 m to 0.004 m. Accordingly, there were detected three times inflation-deflation periods termed as crest preceding the eruption. The three crests were precursory signal started on November 2008 (first crest), November 2009 (second crest), and July 2010 (third crest). The paroxysmal third crest was successfully identified at the summit of Mount Sinabung by inflation about 1.4 cm prior to the eruptions. Following the eruption, the deflation occurred due to withdrawal of magma pressure fed to the eruption. The three crest periods are indications of magmatic plumbing system from the crust and/or deep magma reservoir about 5.2 - 8.7 km deep from the summit. The migration process of magma batches and dike generations through the subsurface allowed for a graben-like to form presented by the inflation-deflation of ground surface. The low and high soil moisture detected by Sentinel-1A served as an indicator of syn- and intra-eruption periods. In the syn-eruptions, the new volcanic products produced by the eruptions including lava and pyroclastic flow deposits were strongly affected to the moisture content of the surface layer. Evaporation of surface moisture due to surface drying from hot volcanic products decreased the surface moisture. In the intra-eruptions, the surface moisture increased due to infiltration of meteoric water to the pore volcanic products, such as pyroclastics and tephra.

Acknowledgements

The authors thank to anonymous reviewers for their constructive comments improving the quality and clarity of the paper. The ALOS PALSAR and Sentinel-1A SAR data used in this study were provided by Remote Sensing Technology Center of Japan (RESTEC) and Sentinel open access hub (https://scihub.copernicus.eu/dhus/#/home).

References

BKSPN, 2009. *Peta Rupa Bumi Indonesia skala 1:50.000*. Bakosurtanal.

Bodnar, R.J., Cannatelli, C., De Vivo, B., Lima, A., Belkin, H.E., and Milia, A., 2007. Quantitative model for magma degassing and ground deformation (bradyseism) at Campi Flegrei, Italy: Implications for future eruptions. *Geology,* 35, p. 791-794. DOI:10.1130/g23653a.1

Box, J.E., Sletten, W.H., Kyle, J.H., and Pope, A., 1963. Effects of soil moisture, temperature, and fertility on yield and quality of irrigated potatoes in the Southern Plains. *Agronomy Journal,* 55, p.492-494. DOI:10.2134/agronj1963.00021962005500050025x

Campbell, B.A. and Garvin, J.B., 1993. Lava flow topographic measurements for radar data interpretation. *Geophysical Research Letters,* 20, p.831-834. DOI:10.1029/93gl00737

Chaussard, E. and Amelung, F., 2012. Precursory inflation of shallow magma reservoirs at west Sunda volcanoes detected by InSAR. *Geophysical Research Letters,* 39(L21311),p.1-6. DOI:10.1029/2012gl053817

Cronin, S.J., Hedley, M.J., Neall, V.E., and Smith, R.G., 1998. Agronomic impact of tephra fallout from the 1995 and 1996 Ruapehu Volcano eruptions, New Zealand. *Environmental Geology,* 34, p.21-30. DOI:10.1007/s002540050253

Das, K. and Paul, P.K., 2015. Soil moisture retrieval model by using RISAT-1, C-band data in tropical dry and sub-humid zone of Bankura district of India. *The Egyptian Jour-*

nal of Remote Sensing and Space Science, 18, p.297-310. DOI:10.1016/j.ejrs.2015.09.004

De Roo, R.D., Du, Y., Ulaby, F.T., and Dobson, M.C., 2001. A semi-empirical backscattering model at L-band and C-band for a soybean canopy with soil moisture inversion. *IEEE Transactions on Geoscience and Remote Sensing,* 39, p.864-872. DOI:10.1109/36.917912

Dubois, P.C., Van Zyl, J., and Engman, T., 1995. Measuring soil moisture with imaging radars. *IEEE Transactions on Geoscience and Remote Sensing,* 33, p.915-926. DOI:10.1109/36.406677

Einarsson, P. and Brandsdottir, B., 1978. *Seismological evidence for lateral magma intrusion during the July 1978 deflation of the Krafla volcano in NE-Iceland*. University of Iceland, Reykjavik, IS. DOI:10.2172/890964

Gharechelou, S., Tateishi, R., and Sumantyo, J.T.S., 2015. Interrelationship analysis of L-band backscattering intensity and soil dielectric constant for soil moisture retrieval using PALSAR data. *Advances in Remote Sensing,* 4, p.15. DOI:10.4236/ars.2015.41002

Gong, W., Meyer, F., Webley, P.W., and Lu, Z., 2011. Methods of INSAR atmosphere correction for volcano activity monitoring. *IEEE International Geoscience and Remote Sensing Symposium (IGARSS)*, p.1654-1657. DOI:10.1109/igarss.2011.6049550

González, P.J., Singh, K.D., and Tiampo, K.F., 2015. Shallow Hydrothermal Pressurization before the 2010 Eruption of Mount Sinabung Volcano, Indonesia, Observed by use of ALOS Satellite Radar Interferometry. *Pure and Applied Geophysics,* 172, p.3229-3245. DOI:10.1007/s00024-014-0915-7

Gunawan, H., Budianto, A., Prambada, O., McCausland, W., Pallister, J., and Iguchi, M., 2017. Overview of the eruptions of Sinabung eruption, 2010 and 2013-present and details of the 2013 phreatomagmatic phase. *Journal of Volcanology and Geothermal Research*, In press,p.1-17. DOI:10.1016/j.jvolgeores.2017.08.005

Hanssen, R.F., 2001. *Radar Interferometry: Data Interpretation and Error Analysis*. Kluwer Academic Publishers, Dordrecht, 308pp. DOI:10.1007/0-306.47633-9

Hirschi, M., Seneviratne, S.I., Alexandrov, V., Boberg, F., Boroneant, C., Christensen, O.B., Formayer, H., Orlowsky, B., and Stepanek, P., 2011. Observational evidence for soil-moisture impact on hot extremes in southeastern Europe. *Nature Geoscience,* 4, p.17-21. DOI:10.1038/ngeo1032

Iguchi, M., Ishihara, K., and Hendrasto, M., 2011. Learn from 2010 eruptions at Merapi and Sinabung volcanoes in Indonesia, *Proceedings of Annuals of Disaster Prevention Research Institute*. Kyoto University, Kyoto, p.1-10.

Iguchi, M., Nishimura, T., Hendrasto, M., Rosadi, U., Ohkura, T., Triastuty, H., Basuki, A., Loeqman, A., Maryanto, S., and Ishihara, K., 2012. Methods for eruption prediction and hazard evaluation at Indonesian volcanoes. *Journal of Disaster Research,* 7, p.26-36. DOI:10.20965/jdr.2012.p0026

Indrastuti, N., Nugraha, A.D., McCausland, W.A., Hendrasto, M., Gunawan, H., and Kusnandar, R., 2019. 3-D seismic tomographic study of Sinabung Volcano, Northern Sumatra, Indonesia, during the inter-eruptive period October 2010–July 2013. *Journal of Volcanology and Geothermal Research*, In Press. DOI:10.1016/j.jvolgeores.2019.03.001

Kriswati, E., Kuncoro, H., and Meilano, I., 2015. Low rate of Sinabung deformation inferred by GPS measurement, *AIP Conference Proceedings*. AIP Publishing, p.050007. https://doi.org/10.1063/1.4915046. DOI:10.1063/1.4915046.

Lanari, R., Casu, F., Manzo, M., Zeni, G., Berardino, P., Manunta, M., and Pepe, A., 2007. An overview of the small baseline subset algorithm: A DInSAR technique for surface deformation analysis. *Pure and Applied Geophysics,* 164, p.637-661. DOI:10.1007/s00024-007-0192-9

Lee, C.W., Lu, Z., and Kwoun, O.I., 2007. SAR measurements of surface displacements at Augustine volcano, Alaska from 1992 to 2005. *IEEE International Geoscience and Remote Sensing Symposium*

(IGARSS), p. 4671-4674. DOI:10.1109/igarss.2007.4423901

Li, Z., Fielding, E.J., Cross, P., and Preusker, R., 2009. Advanced InSAR atmospheric correction: MERIS/MODIS combination and stacked water vapour models. *International Journal of Remote Sensing,* 30, p.3343-3363. DOI:10.1080/01431160802562172

Li, Z., Muller, J.P., Cross, P., and Fielding, E.J., 2005. Interferometric synthetic aperture radar (InSAR) atmospheric correction: GPS, Moderate Resolution Imaging Spectroradiometer (MODIS), and InSAR integration. *Journal of Geophysical Research: Solid Earth 110*. https://doi.org/10.1029/2004JB003446. DOI:10.1029/2004JB003446.

Lu, Z., Masterlark, T., and Dzurisin, D., 2005. Interferometric synthetic aperture radar study of Okmok volcano, Alaska, 1992–2003: Magma supply dynamics and postemplacement lava flow deformation. *Journal of Geophysical Research: Solid Earth,* 110(B2), p.1-18. DOI: 10.1029/2004JB003148. DOI:10.1029/2004jb003148

Martí, J. and Ernst, G., 2005. *Volcanoes and the Environment*. Cambridge University Press, 471pp.

Massonnet, D. and Feigl, K.L., 1998. Radar interferometry and its application to changes in the Earth's surface. *Reviews of Geophysics,* 36, p.441-500. DOI: 10.1029/97RG03139

Mastin, L.G. and Pollard, D.D., 1988. Surface deformation and shallow dike intrusion processes at Inyo Craters, Long Valley, California. *Journal of Geophysical Research: Solid Earth,* 93, p.13221-13235. DOI:10.1029/jb093ib11p13221

Nakada, S., Zaennudin, A., Yoshimoto, M., Maeno, F., Suzuki, Y., Hokanishi, N., Sasaki, H., Iguchi, M., Ohkura, T., and Gunawan, H., 2017. Growth process of the lava dome/flow complex at Sinabung Volcano during 2013-2016. *Journal of Volcanology and Geothermal Research,* 17pp. DOI: 10.1016/j.jvolgeores.2017.06.012

Nugraha, A.D., Indrastuti, N., Kusnandar, R., Gunawan, H., McCausland, W., Aulia, A.N., and Harlianti, U., 2017. Joint 3-D tomographic imaging of Vp, Vs and Vp/Vs and hypocentre relocation at Sinabung volcano, Indonesia from November to December 2013. *Journal of Volcanology and Geothermal Research.* DOI: 10.1016/j.jvolgeores.2017.09.018

Nugraha, A.D., Supendi, P., Widiyantoro, S., Daryono, and Wiyono, S., 2018. Earthquake swarm analysis around Bekancan area, North Sumatra, Indonesia using the BMKG network data: Time periods of February 29, 2015 to July 10, 2017, *AIP Conference Proceedings.* AIP Publishing, p. 020092. DOI:10.1063/1.5047377

Nugroho, S.P., 2013. Riwayat Letusan Sinabung. *Gema BNPB,* 4, p.42-45.

Ozdarici, A. and Akyurek, Z., 2010. A comparison of SAR filtering techniques on agricultural area identification. *Proceedings of ASPRS 2010 Annual Conference, California*, p. 26-30.

Papageorgiou, E., Foumelis, M., and Parcharidis, I., 2012. Long-and short-term deformation monitoring of Santorini Volcano: Unrest evidence by DInSAR analysis. *IEEE Journal of Selected Topics in Applied Earth Observations and Remote Sensing,* 5, p.1531-1537. DOI:10.1109/jstars.2012.2198871

Peng, Y., Shen, C., Wang, W.C., and Xu, Y., 2010. Response of summer precipitation over Eastern China to large volcanic eruptions. *Journal of Climate,* 23, p.818-824. DOI:10.1175/2009jcli2950.1

Rosen, P.A., Hensley, S., Zebker, H.A., Webb, F.H., and Fielding, E.J., 1996. Surface deformation and coherence measurements of Kilauea Volcano, Hawaii, from SIR-C radar interferometry. *Journal of Geophysical Research: Planets,* 101, p.23109-23125. DOI:10.1029/96je01459

Saepuloh, A., Koike, K., and Omura, M., 2012. Applying Bayesian Decision Classification to Pi-SAR polarimetric data for detailed extraction of the geomorphologic and structural features of an active volcano. *IEEE Geoscience and Remote Sensing Letters,* 9, p.554-558. https://doi.org/10.1109/LGRS.2011.2174611.

Saepuloh, A., Koike, K., Omura, M., Iguchi, M., and Setiawan, A., 2010. SAR- and gravity change-based characterization of the distribution pattern of pyroclastic flow deposits at Mount Merapi during the past 10 years. *Bulletin of Volcanology,* 72, p.221-232. DOI:10.1007/s00445-009-0310-x.

Saepuloh, A., Koike, K., Urai, M., and Sumantyo, J.T.S., 2015a. Identifying surface materials on an active volcano by deriving dielectric permittivity from polarimetric SAR data. *IEEE Geoscience and Remote Sensing Letters,* 12, p.1620-1624. DOI:10.1109/LGRS.2015.2415871.

Saepuloh, A., Susanto, A., Sumintadireja, P., and Suparka, E., 2015b. Characterizing surface manifestation of geothermal system under Torrid Zone using Synthetic Aperture Radar (SAR) data, *Proceedings of the World Geothermal Congress 2015.* Melbourne, Australia, p.1-6.

Saepuloh, A., Urai, M., Aisyah, N., Sunarta, Widiwijayanti, C., Subandriyo, and Jousset, P., 2013. Interpretation of ground surface changes prior to the 2010 large eruption of Merapi volcano using ALOS/PALSAR, ASTER TIR and gas emission data. *Journal of Volcanology and Geothermal Research, Merapi eruption,* 261, p.130-143. DOI:10.1016/j.jvolgeores.2013.05.001.

Saepuloh, A., Wikantika, K., and Urai, M., 2015c. Observing lava dome roughness on Synthetic Aperture Radar (SAR) data: Case study at Mount Sinabung and Merapi - Indonesia, *2015 IEEE 5th Asia-Pacific Conference on Synthetic Aperture Radar (APSAR)*. Presented at the 2015 IEEE 5th Asia-Pacific Conference on Synthetic Aperture Radar (APSAR), p. 645-648. DOI:10.1109/APSAR.2015.7306289.

Schmincke, H.-U., 2004. *Volcanism,* 28. Springer Science & Business Media, 324pp.

Sigmundsson, F., Einarsson, P., and Bilham, R., 1992. Magma chamber deflation recorded by the Global Positioning System: The Hekla 1991 eruption. *Geophysical Research Letters,* 19, p.1483-1486. DOI:10.1029/92gl01636

Song, K., Zhou, X., and Fan, Y., 2010. Retrieval of soil moisture content from microwave backscattering using a modified IEM model. *Progress In Electromagnetics Research B,* 26, p.383-399. DOI:10.2528/pierb10072905

Soussa, J.J., Ruiz, A.M., Hanssen, R.F., Bastos, L., Gil, A.J., Galindo-Zaldívar, J., and de Galdeano, C.S., 2010. PS-InSAR processing methodologies in the detection of field surface deformation-Study of the Granada basin (Central Betic Cordilleras, southern Spain). *Journal of Geodynamics,* 49, p.181-189. DOI:10.1016/j.jog.2009.12.002.

Sutawidjaja, I.S., Prambada, O., and Siregar, D.A., 2013. The August 2010 Phreatic Eruption of Mount Sinabung, North Sumatra. *Indonesian Journal on Geoscience,* 8, p.55-61. DOI:10.17014/ijog.v8i1.155

Topp, G.C., Davis, J.L., and Annan, A.P., 1980. Electromagnetic determination of soil water content: Measurements in coaxial transmission lines. *Water Resources Research,* 16, p.574-582. DOI:10.1029/wr016i003p00574

Trenberth, K.E. and Dai, A., 2007. Effects of Mount Pinatubo volcanic eruption on the hydrological cycle as an analog of geoengineering. *Geophysical Research Letters,* 34(L15702, p.1-5. DOI: 10.1029/2007GL030524

Witra, T., Saepuloh, A., Harto, A.B., and Wikantika, K., 2017. Analyzing surface roughness models derived by SAR and DEM data at geothermal fields. *Bulletin of Geology,* 1, p.77-85. DOI:10.5614/bull.geol.2017.1.2.1

Wyrick, D.Y. and Smart, K.J., 2009. Dike-induced deformation and Martian graben systems. *Journal of Volcanology and Geothermal Research,* 185, p.1-11. DOI:10.1016/j.jvolgeores.2008.11.022

Zampieri, M., D'Andrea, F., Vautard, R., Ciais, P., de Noblet-Ducoudré, N., and Yiou, P., 2009. Hot European summers and the role of soil moisture in the propagation of Mediterranean drought. *Journal of Climate,* 22, p.4747-4758. DOI:10.1175/2009jcli2568.1

Zribi, M. and Dechambre, M., 2003. A new empirical model to retrieve soil moisture and roughness from C-band radar data. *Remote Sensing of Environment,* 84, p.42-52. DOI:10.1016/s0034-4257(02)00069-x